Vision, Modeling, and Visualization (2018)
F. Beck, C. Dachsbacher, and F. Sadlo (Eds.)

Efficient Subsurface Scattering Simulation for Time-of-Flight Sensors

David Bulczak and Andreas Kolb
Computer Graphics Group, Institute for Vision and Graphics (IVG), University of Siegen, Germany

Abstract

Today, amplitude modulated continuouswave (AMCW) Time-of-Flight (ToF) range cameras are ubiquitous devices that are employed in many fields of application, such as robotics, automotive industry, and home entertainment. Compared to standard RGB cameras, ToF cameras suffer from various error sources related to their fundamental functional principle, such as multipath interference, motion artifacts, or subsurface scattering. Simulating ToF cameras is essential in order to improve future ToF devices or to predict their operability in specific application scenarios. In this paper we present a first simulation approach for ToF cameras that incorporates subsurface scattering effects in semi-transparent media. Subsurface scattering significantly alters the optical path length measured by the ToF camera, leading to erronous phase calculations and, eventually, to wrong range values. We address the challenge to efficiently simulate the superimposed light paths regarding intensity and phase. We address a restricted constellation, i.e., a single semi-transparent layer located on top of an opaque object. Our interactive screen-space AMCW ToF simulation technique incorporates a two-pass light scattering propagation, involving the forward and backward scattering at the interface between air and the semi-transparent object, taking amplitude and phase variations into account. We evaluate our approach by comparing our simulation results to real-world measurements.

1. Introduction

Todays most common range sensing camera type is based on the amplitude modulated continuous wave (AMCW) Time-of-Flight (AMCW-ToF) principle. AMCW-ToF cameras acquire depth information on a per-pixel basis by estimating the phase shift of an amplitude modulated light signal travelling from the camera's active light source to the object and back to the camera pixel. The determined phase shift is propotional to the time, thus, to the distance the light travels anlong this path. The working principle of AMCW ToF cameras induces several error sources related to the resulting distance measurements such as motion artifacts, flying pixels, multipath interference (MPI) and subsurface scattering.

The simulation of AMCW ToF cameras is important in order to, e.g., improve these devices by varying the chip design and parametrization [LHK15], to evaluate applications like object detection, or by providing synthetic and ground truth data [NML*13]. Therefore, it is of high importance that a simulation captures the aforementioned major sensor effects by proper modeling of the illumination, the light transfer within the scene as well as individual sensor pixel behavior. Furthermore, computational efficiency plays an essential role, as many algorithms address dynamic scenes as well and parameter evaluation or machine learning require the generation of a large variety of simulated test data. Recent developments in ToF simulation address multipath interference [MNK13], for which Bulczak et al. [BLK17] developed an interactive variant.

To the best of our knowledge subsurface scattering effects have not been addressed so far in the context of ToF camera simulation. Subsurface scattering, however, has a strong influence on the accuracy of the distance measurement, which may be very critical in safety applications in which semi-transparent materials occur. Examples are human-robot interaction or food production. There is a lot of prior research that addresses the processing of ToF data and the elemination of such error effects e.g. [MHM*18], [SHWH18]. This paper doesn't consider handling such errors.

In this paper we present a first approach to simulate subsurface scattering effects for AMCW ToF cameras. Our approach is a physically motivated, interactive screen space approach, and is fully GPU-based. We efficiently simulate the superimposed light paths in scattering media explicitly modeling intensity and phase. In order to achieve interactive frame-rates, we restrict our simulation to a single semi-transparent layer located on top of an opaque object. Our simulation technique incorporates a two-pass light scattering propagation involving the forward and backward scattering at the interface between air and the semi-transparent object, taking amplitude and phase variations into account. It accounts for the spatial distribution of light energy within semi-transparent materials, Fresnel reflexion and transmission, as well as the scattering along light rays using phase functions.

DOI: 10.2312/vmv.20181259

2. Related Work

On the physical level, light transport in arbitrary scattering media can be accurately simluated by solving the radiative transfer equation [Ish78]. In computer graphics, ray tracing and radiosity approaches have been used that incorporate volumetric Monte Carlo or finite element techniques [Max95,RT87]. Since the simulation of multiple volumetric scattering effects is extremely costly, various research has been initiated in order to come up with more efficient approaches.

Jensen et al. [JMLH01] propose a fast approximation of the scattering simulation consisting of a single scattering component, a diffusion term, and a Fresnel term. While the single scattering term computes scattering in case the refracted light ray and the refracted viewing ray intersect, diffusion approximation involves a dipole model in order to describe radiance distribution. Donner et al. [DLR*09] approximate the 8-dimensional bidirectional scattering surface reflectance distribution function (BSSRDF) that models volumetric scattering as a function, parametrized over the incidence and existence points and directions of the light. They use an empirical photon tracing approach based on a large variety of simulated material configurations resulting in a 2D hemispherical distribution of exitant light direction. Premože et al. [PAT*04] suggest a point spread function that captures blurring of radiance due to multiple scattering in the semi-transparent volume, leading to a 2D filter approach. They use a path integral method that samples along the viewing ray and integrates the radiance based on the blur distribution with respect to the path length toward the light source. Elek et al. [ERS13] adopt Premože et al.'s method to screen-space. Their algorithm approximates light scattering in homogeneous participating media and uses an efficient hierarchical convolution applied to texture MIP maps. Jimenez et al. [JZJ*15] present a screen-space approach that defers the blurring until the shading is computed in order to maintain geometric details as long as possible. [NAM*17] et al. present a modern deep learning based real-time rendering method that covers several effects like diffuse indirect light and sub-surface scattering.

Regarding our priliminary goal of an interactive subsurface simulation of intensity and phase for a single semi-transparent layer, the discussed methods have two main limitations: Either they use radiance transfer models that can handly be adopted to handle phase [DLR*09,JMLH01,JZJ*15,ERS13] or that are computationally too exhaustive [PAT*04].

3. 2-Tap AMCW ToF in a Nutshell

Time-of-Flight (ToF) cameras calculate the camera-object distance d by estimating the time delay t that actively emitted light takes to travel from the light source to the object surface and back to the sensor's pixel (see Fig. 1):

$$d = \frac{1}{2} \cdot c \cdot t, \tag{1}$$

where c is the speed of light.

Amplitude-modulated continuous-waves (AMCW) ToF cameras emit an intensity modulated light signal in the near infrared range and measure the phase shift of this signal while arriving at the sensor; see Fig. 1. For this purpose the received optical signal s is correlated with the reference signal g which controls the active light modulation:

$$C(\Delta\phi) = s \otimes g = \lim_{T\to\infty} \int_{-\frac{T}{2}}^{\frac{T}{2}} s(t)g(t+\Delta\phi)\,dt, \tag{2}$$

where $\Delta\phi$ is a controllable internal phase delay. Assuming a sinusoidal signal we get

$$C(\Delta\phi) = \frac{a}{2}\cos(f_{mod}\Delta\phi + \phi) + b \tag{3}$$

with modulation frequency f_{mod}, correlation amplitude a and bias b, and phase shift

$$\phi = 4\pi d \frac{f_{mod}}{c}. \tag{4}$$

Commonly, $C(\Delta\phi)$ is sampled at four different phase shifts $\Delta\phi = i \cdot \frac{\pi}{2}, i \in \{0,1,2,3\}$ yielding so-called *phase images* $D_i = C(i \cdot \frac{\pi}{2})$ to

$\mathcal{T}, \mathcal{M}, \mathcal{O}$	the air-translucent interface, the translucent media, the opaque surface
T	point on transparent surface
M	point within transparent surface
O	point on opaque surface
$T_0 \to T_1 \to \ldots \to T_n$	path of length n from T_0 to T_n
$\vec{\mathbf{L}}^r_{\text{path}} = L_{\text{path}} \cdot e^{i\phi^c_{\text{path}}}$	reflectance radiance phasor of path
$\vec{\mathbf{L}}^s_{\text{path}} = L_{\text{path}} \cdot e^{i\phi^c_{\text{path}}}$	scattering radiance phasor of path
L_{path}	radiance along path
ϕ^c_{path}	phase shift resulting from path
$F^r_{I\to P\to O}$	reflective Fresnel at P from I to O
$F^t_{I\to P\to O}$	transmissive Fresnel at P from I to O
$f_{I\to P\to O}$	BRDF at P from I and to O
σ_a, σ_s	absorption and scattering coefficient
$p(\theta)$	phase function
g	anisotropy factor of phase function
c, c_A, c_M	speed of light, in air and in translucent media
$\eta = c_A/c_M$	relative refraction index
f_{mod}	ToF modulation frequency
$d(P_1, P_2)$	distance between P_1 and P_2
t	offset value that defines $M \in \mathcal{M}$ for a given pixel

Table 1: *Notations used in this paper.*

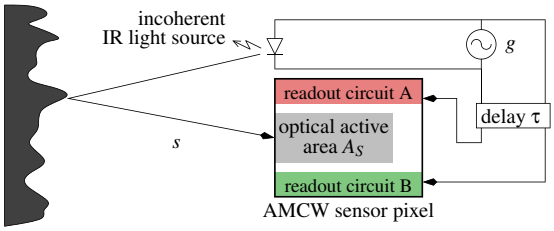

Figure 1: *Scheme of a AMCW ToF camera*

regain the actual phase shift with

$$\phi = \text{atan2}(D_3 - D_1, D_0 - D_2). \tag{5}$$

2-tap hardware implementations of this AMCW ToF principle, such as the *Photonic Mixing Device (PMD)* cameras [Inf15], use two readout circuits A and B in order to collect all photon generated electrons (see Fig. 1). Formally, both the correlation function $C(\Delta\phi)$ and its inverse $C(\Delta\phi+\pi)$ are sampled at the same time, which could be used to reduce the number of phase image acquisitions to two. Practically, however, all four samples are taken and in each acquisition the difference of two gate charges N_A, N_B is used to compute the phase image $D_i = N_{A,i} - N_{B,i}$. This approach leads to more robust estimations of ϕ as inhomogeneities in hardware, e.g. the pixel gains in A and B, are canceled out.

4. Time-of-Flight Simulation with Subsurface Scattering

In this section a model for radiance transfer in transparent media is presented. The scenario under consideration consists of a semi-transparent layer on top of an opaque layer and a Time-of-Flight camera positioned above. The goal is to simulate the intensity L and the phase shift ϕ of the amplitude modulated light that arrives at the sensor C (see Eq. 4). Using a complex phasor notation $\vec{\mathbf{L}} = L \cdot e^{i\phi}$ to denoted both quantities, the initial situation at the light source is given as $\vec{\mathbf{L}}_C = L_C \cdot e^{i\cdot 0}$.

We denote $\mathcal{T}, \mathcal{M}, \mathcal{O}$ as the interface (surface) between air and the semi-transparent material, the volume of the semi-transparent media, and the surface of the underlying opaque material, respectively. We have to consider the resulting phasor $\vec{\mathbf{L}}_{L\to\ldots\to C}$ after the light traveled the path $L \to \ldots \to C$ from the light source L to C. As we assume a single scattering event in the participating media or at the opaque surface $\mathcal{O}$, the phasor that arrives at the camera C is a superposition of radiance resulting from direct reflection at $\mathcal{T}$, radiance that is reflected within the transparent material $\mathcal{M}$ and light that gets reflected on the opaque surface $\mathcal{O}$. Thus, the total phasor incident at a camera pixel that observes $T \in \mathcal{T}$ is given by

$$\begin{aligned}\vec{\mathbf{L}}_C^{\text{in}} = &\vec{\mathbf{L}}^r_{L\to T\to C} \\ &+ \int_{T'\in\mathcal{T}} \int_{M\in\mathcal{M}\cap\mathcal{R}_T} \vec{\mathbf{L}}^s_{L\to T'\to M\to T\to C}\, dM\, dT' \\ &+ \int_{T'\in\mathcal{T}} \vec{\mathbf{L}}^r_{L\to T'\to O\to T\to C}\, dT',\end{aligned} \tag{6}$$

We restrict the back-scattering to the sensor to $\mathcal{R}_T \subset \mathcal{M}$, which is the viewing ray refracted at T; see Fig. 2.

According to Eq. 4 the phase shift depends on the speed of light in air c_A or in the transparent material c_M. Given the modulation frequency f_{mod} of the ToF camera. A phase shift $\phi^c_{T_1\to T_2}$ along the linear path segment in a homogeneous material with homogeneous speed to light c_1 is given by

$$\phi^c_{T_1\to T_2} = \frac{2\pi f_{\text{mod}}}{c_1} \cdot d(T_1, T_2). \tag{7}$$

For a given discrete light path $T_0 \to T_1 \to \ldots \to T_n$, piecewise constant speed of light and absorption (c_i and $\sigma_{a,i}$ on $T_i \to T_{i+1}$)

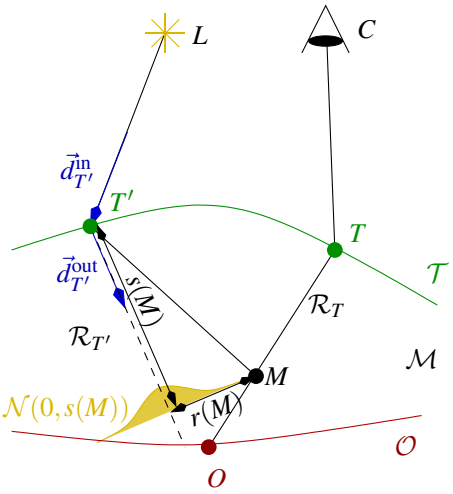

Figure 2: *Path scattering model.*

and the initial phasor $\vec{\mathbf{L}}_0$, the resulting phasor at T_n is

$$\vec{\mathbf{L}}_{T_0\to T_n} = \vec{\mathbf{L}}_0 \prod_{j=1}^{n-1} \vec{\mathbf{L}}_{T_j\to T_{j+1}}, \quad \vec{\mathbf{L}}_{T_j\to T_{j+1}} = e^{-\tau_{T_j\to T_{j+1}}} \cdot e^{i\phi^c_{T_j\to T_{j+1}}}, \tag{8}$$

where $\tau_{T_j\to T_{j+1}} = \sigma_{a,j} \cdot d(T_j, T_{j+1})$ is the optical depth. Here, $e^{-\tau_{T_j\to T_{j+1}}}$ denotes the damping due to absorption and $e^{i\phi^c_{T_j\to T_{j+1}}}$ the phase delay within the material.

4.1. Direct Light Propagation

The direct reflection (first term in Eq. 6) can be expressed by common radiance reflection models e.g.

$$\begin{aligned}\vec{\mathbf{L}}^r_{L\to T\to C} &= L_{L\to T\to C} \cdot e^{i\cdot\phi_{L\to T\to C}} \\ &= \vec{\mathbf{L}}_{L\to T} \cdot f_{L\to T\to C} \cdot \cos(\omega^{in}_T) \cdot e^{i\cdot\frac{2\pi f_{\text{mod}}}{c_A}\cdot(d(T,L)+d(C,T))},\end{aligned} \tag{9}$$

where $f_{L\to T\to C}$ denotes the corresponding BRDF, T and ω^{in}_T the angle of incident light at T. Note that in our model the BRDF $f_{L\to T\to C}$ includes a Fresnel reflection factor F^r. Here, we assume the absorption in air to be 0, thus no damping occurs.

4.2. Light Propagation in Transparent Materials

Computing the second term in Eq. 6 requires to calculte the phasor $\vec{\mathbf{L}}_{L\to T'\to M}$ for given $T' \in \mathcal{T}, M \in \mathcal{M}$. Given the incident light direction $\vec{d}^{\text{in}}_{T'} = (T' - L)/d(T', L)$, the Fresnel refraction factor $F^t_{\vec{d}^{\text{in}}_{T'}\to\vec{d}^{\text{out}}_{T'}}$ describes the relative amount of radiance refracted in the outgoing light direction $\vec{d}^{\text{out}}_{T'}$; see Fig. 2. We discribe the scattering behaviour in semi-transparent media using the Henyey-Greenstein phase function [HG41]:

$$p(\theta) = \frac{1}{4\pi} \frac{1-g^2}{\left[1+g^2-2g\cos\theta\right]^{\frac{3}{2}}}. \tag{10}$$

Here, θ is the scattering angle between the incident light direction at a scattering point $M \in \mathcal{M}$ and the outgoing direction, and $g \in$

$[-1,1]$ controls the scattering behaviour from backscattering ($g=-1$), via isotropic scattering ($g=0$) to forward scattering ($g=1$). Please note that the term "phase function" relates to scattering in translucent media, while "phase shift" relates to the travelling time of amplitude modulated light (see Eq. 4), i.e., they are independent.

Based on the phase function, Premože and colleagues derive a Gaussian 3D distribution [PAT*04]. The standard deviation of this 3D Gaussian lateral to the incident light direction is given as:

$$W(s)=\sqrt{\frac{1}{2}\left(\frac{\sigma_a}{3s}+\frac{4}{s^3\sigma_s(1-g)}\right)^{-1}}, \tag{11}$$

where s is the distance the light traveled in the media. Finally, we can deduce the required phasor as:

$$\vec{\mathbf{L}}_{L\to T'\to M}= \tag{12}$$
$$\vec{\mathbf{L}}_{L\to T'}\cdot F^t_{\vec{d}^{\text{in}}_{T'}\to\vec{d}^{\text{out}}_{T'}}\cdot\mathcal{N}_{0,W(s(M))}(r(M))\cdot e^{-\sigma_a d(T',M)}e^{i\phi_{T'\to M}},$$

where $\mathcal{N}_{\mu,\sigma}$ is the normal distribution with mean μ and standard deviation σ, $s(M)=\left\langle \vec{d}^{\text{out}}_{T'} \mid (M-T')\right\rangle$ is the projected distance of $M-T'$ onto $\vec{d}^{\text{out}}_{T'}$ and $r(M)=\left\|(M-T')-s(M)\vec{d}^{\text{out}}_{T'}\right\|$ is the distance of M to the light ray with direction $\vec{d}^{\text{out}}_{T}$; see Fig. 2. $\vec{\mathbf{L}}_{L\to T'\to S}$, $O\in\mathcal{O}$ can also be computed according to Eq.12.

The second parts of $\vec{\mathbf{L}}^s_{L\to T'\to M\to T\to C}$ and of $\vec{\mathbf{L}}^r_{L\to T'\to O\to T\to C}$ are computed as follows

$$\vec{\mathbf{L}}_{M\to T\to C}=e^{-\sigma_a d(M,T)}\cdot F^t_{\vec{d}^{\text{in}}_{T}\to\vec{d}^{\text{out}}_{T}}\cdot e^{i(\phi^{cM}_{M\to T}+\phi^{ca}_{T\to C})}, \tag{13}$$

$$\vec{\mathbf{L}}_{O\to T\to C}=e^{-\sigma_a d(O,T)}\cdot F^t_{\vec{d}^{\text{in}}_{T}\to\vec{d}^{\text{out}}_{T}}\cdot e^{i(\phi^{cM}_{O\to T}+\phi^{ca}_{T\to C})}. \tag{14}$$

Finally, the total light and phase transport is combined as:

$$\vec{\mathbf{L}}_{L\to T'\to M\to T\to C}=\vec{\mathbf{L}}_{L\to T'\to M}\cdot p(\theta)\cdot\vec{\mathbf{L}}_{M\to T\to C}, \tag{15}$$

$$\vec{\mathbf{L}}_{L\to T'\to O\to T\to C}=\vec{\mathbf{L}}_{L\to T'\to O}\cdot f_{T'\to O\to T}\cdot\cos(\omega^{in}_O)\cdot\vec{\mathbf{L}}_{O\to T\to C}. \tag{16}$$

Here, we keep the volume scattering and the reflection modeled by the phase function $p(\theta)$ and the BRDF $f_{T'\to O\to T}$ separate, as they relay on the ingoing and outgoing light directions at M and O, respectively.

5. Screen Space Subsurface Scattering

In our screen space approach we untilize G-Buffers to implement the subsurface scattering models presented in Sec. 4 in a deferred rendering setup. We use a two layered buffer where the first layer contains data correspoding to $\mathcal{T}$ while the second layer stores information correspoding to $\mathcal{O}$. Thus we perform the following steps

1. Render G-Buffer $\mathcal{B}_T$ containing data related to $\mathcal{T}$
2. Render G-Buffer $\mathcal{B}_O$ containing data related to $\mathcal{O}$
3. Render final image

Alg. 1 summarizes the computation. The main idea is to sample a single point $M\in\mathcal{M}$ on $\mathcal{R}_T$ for each point $T\in\mathcal{T}$ observed by a pixel in screenspace, for which we gather scattered light from all observed points $T'\in\mathcal{T}$ stored in buffer $\mathcal{B}_T$. Sec. 5.1 describes the information stored in $\mathcal{B}_T$ and $\mathcal{B}_O$. Sec. 5.2 discusses the selection of the sampling point M and the blending scheme that combines scattering in the media and ob the underlying opaque surface.

Executed for each pixel $T\in\mathcal{B}_T$ on shader
Input:
$\mathcal{B}_T$: G-Buffer corresponding to $\mathcal{T}$ ▷ Sec. 5.1
$\mathcal{B}_O$: G-Buffer corresponding to $\mathcal{O}$ ▷ Sec. 5.1
ε: threshold
  $\vec{\mathbf{L}}_L\leftarrow L_L\cdot e^{i\cdot 0}$ ▷ initial phasor starting at L
  for all $O\in\mathcal{B}_O$ **do**
    $M\leftarrow$ selectSamlingPoint(T,O) ▷ Sec. 5.1
    $\vec{\mathbf{L}}^{\text{direct}}\leftarrow\vec{\mathbf{L}}_C\cdot$computeDirectReflection() ▷ Eq. 9
    $\vec{\mathbf{L}}^{\text{scatter}}\leftarrow 0$ ▷ total scattering in M,O
    for all $T'\in\mathcal{B}_T$ **do**
      $\vec{\mathbf{L}}_{L\to M\to C}\leftarrow$ calc. $\vec{\mathbf{L}}_{L\to T'\to M\to T\to C}$ ▷ see Eq.15
      if $d(M,O)<\varepsilon$ **then** ▷ Blending required
        $\vec{\mathbf{L}}_{L\to O\to C}\leftarrow$ calc. $\vec{\mathbf{L}}_{L\to T'\to O\to T\to C}$ ▷ Eq.16
        $\vec{\mathbf{L}}^{\text{scatter}}+=\text{blend}(\vec{\mathbf{L}}_{L\to M\to C},\vec{\mathbf{L}}_{L\to O\to C})$
      else
        $\vec{\mathbf{L}}^{\text{scatter}}+=\vec{\mathbf{L}}_{L\to M\to C}$
      end if
    end for
  end for
  return $\vec{\mathbf{L}}^{\text{direct}}+\vec{\mathbf{L}}^{\text{scatter}}$ ▷ final phasor arriving at L

Algorithm 1: Pseudocode of computation of radiance for each pixel.

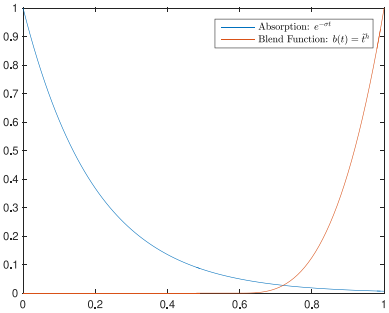

Figure 3: *Schematic plot of the absorption function with* $\sigma=5$ *and the blending function* $b(t)$ *for* $h=3$ *and a threshold distance* $\varepsilon=0.4$.

5.1. Data Buffers $\mathcal{B}_T$ and $\mathcal{B}_O$

$\mathcal{B}_T$ contains data related to radiance entering the transparent medium at $\mathcal{T}$ that is needed for further scattering computation. We store positions and normals in world coordinates as well as the incident radiance intensity and direction. The latter is needed for Fresnel and refraction computations.

This buffer contains the same data as $\mathcal{B}_T$ but correspoding to $O\in\mathcal{O}$ and a single intermediate sampling point $M\in\mathcal{M}$ within the transparent medium. We, again, store position and normal incident radiance intensity and direction for O and offset factor t that defines M. In order to simplify computations, we do not calculate the refracted viewing direction, as this would require the determination of the intersection of the refracted ray with $\mathcal{O}$.

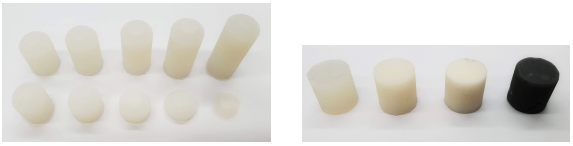

Figure 4: *The left image shows the geometries of different heights used in **Scene 1**. The right image shows the geometry and different materials used in **Scene 2**.*

	σ_a	σ_s	g	η
material #1	18.0	10.0	-0.7	1.6
material #2	20.0	5.0	-0.7	2.0
material #3	35.0	30.0	0.0	2.0
material #4	35.0	8.0	-0.2	2.0

Table 2: *Experimentally determined material properties for base material (**material #1**) and mixed variants.*

5.2. Sampling and Blending Semi-Transparent Media

We position the intermediate sampling point $M \in \mathcal{M}$ using a random offset value t that defines its position as $M = (1-t)T + tO$. The random offset is determined with respect to the absorption σ_a occuring in the transparent material along the path $T \to O$, i.e. t should be small in case of high absorption and vice versa. Thus, we use the absorption function $q(t) = e^{-\sigma_a t}$ as the distribution function for selecting t (see Fig. 3). The cumulative distribution function yields

$$F(t) = \int_0^t q(t')dt' = 1 - e^{-\sigma_a t}. \tag{17}$$

To determine a random offset t we use inverse transform sampling, i.e. we take a uniform random variable $u \in [0,1]$, compute the inverse on F and clamp the resulting value with $d(O,T)$

$$t(u) = \frac{\min\left\{F^{-1}(u), d(T,O)\right\}}{d(T,O)} = \frac{\min\left\{-\frac{ln(1-u)}{\sigma_a}, d(T,O)\right\}}{d(T,O)}. \tag{18}$$

Finally, we compute $M = (1-t)T + tO$. Sampling at M is done according to Eqs.12, 13 and 15; see also Alg. 1.

In case that the sampling point M is close to the correspoding point O on the opaque surface, i.e. $d(M,O) < \varepsilon$, the underlying surface scattering should be taken into account. Therefore, we blend the volume scattered phasor $\vec{\mathbf{L}}_{L\to T'\to M\to T\to C}$ (Eq. 15) and the surface scattered phasor $\vec{\mathbf{L}}_{L\to T'\to O\to T\to C}$ (Eq. 16). We apply the blending function b and normalized parameter $\tilde{t}$, if $d(M,O) < \varepsilon$:

$$b(\tilde{t}) = \tilde{t}^h, \quad \tilde{t} = 1 - \frac{d(M,O)}{\varepsilon}. \tag{19}$$

In our experiments we use $h = 3$ (see Fig. 3).

6. Results

In this section we present an evaluation of the subsurface scattering simulation method presented in the previous sections.

For the acquisition of real world data we use a PMD pico flexx. It captures depth images at 171 x 224 px and uses an active light source that operates at 850 nm wavelength.

For evaluation we prepared three real world scenes with objects consisting of translucent silicone as base material, which we optionally mix with white and black dye in order to achieve different absorption and refraction properties (see figure 4). **Scene 1** consists of multiple cylindrical objects with cap. Their base has a radius 1 cm with varying height. The cylinder's cap is a truncated cone of 0.5 cm height and upper radius of 0.5 cm. The height of the eight base cylinders varies from 0.0 cm to 4.5 cm in 0.5 cm steps. All of the geometries are arranged in two rows with 3 cm lateral distance. **Scene 2** is made of four cylinders of base radius 1.25 cm and height 2.5 cm. In this scene we have mixed the base material with colors to change the scattering properties. The first object is made of the base materials. The second cylinder has slightly changed absorption and scattering properties due to mixed in white color. The third one has strongly changed absorption and scattering properties due to the mixed white color. The last one has strongly changed absorption properties due to mixed in black dye. All cylinders are placed next to each other with 4 cm distance. **Scene 3** uses the cylinders of **Scene 2** but places each cylinder sequentially at exactly the same position. Thus, in this scene the lighting conditions are constant and only the material properties vary. All of the three scenes use a diffuse, opaque white paper as base. In each scene the camera has been positioned to look from the top on the scene but shifted so that the incident light into the objects is not orthogonal. The scenes in our simulation use the same geometry. As we do not have the means to measure the optical properties of our real world object, the material properties have been determined empirically.

Fig. 5 show the comparison of geometry ground truth depth values, i.e. the surface of the translucent objects, as well as the depth values acquired by the pico flexx camera and the results of our simulation. In **Scene 1** large cylinders imply an increase in light path length and thus an major increase in depth values compared to ground truth data. The increase leads to depth values even larger than the depth values of the base plane geometry. Our simulation captures this behavior and delivers results similar to ground truth. **Scene 2** shows that different material properties have a major impact on the resulting depth values. While the base material leads to a large increase in depth estimation all further variants have a less of an effect, due to increased absorption and refraction index which we discuss in more detail.

Scene 3 shows more detailed how the PMD pico flexx behaves for different types of materials and that our simulation model can properly represent these effects. Each version uses the same cylindric geometry but different materials. Figure 6 shows a comparison between geometry ground truth data, our simulationa and pico flexx data. With a lower absorption of $\sigma_a = 18.0$, refraction index of $\eta = 1.6$ and backscattering behavior $g = -0.7$ the base material can be modelled properly. Our simulation provides similar depth behavior as the real world sensor. Increasing the σ_a and slightly η allows to model the behavior of **material # 2**. Due to the mixed in white color the absorption of the material increase. This is reflected also by paramters for **material #3**, i.e. an increased value of the absorption coefficient and a slight adjustment of the scatter-

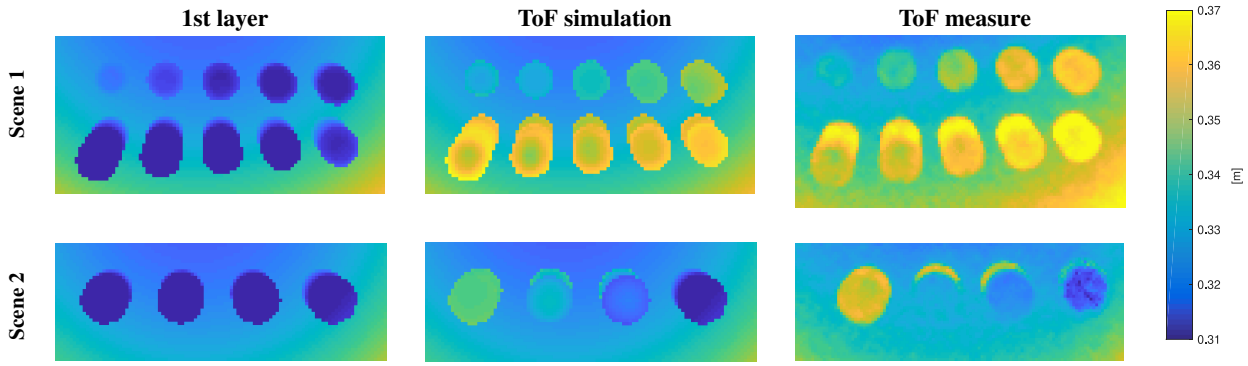

Figure 5: *Comparison of depth images between PMD pico flexx and our simulation in **Scenes 1 & 2**. In all scenes a large increase in depth is visible at the side of the cylinders. Our simulation reflects this behavoir.*

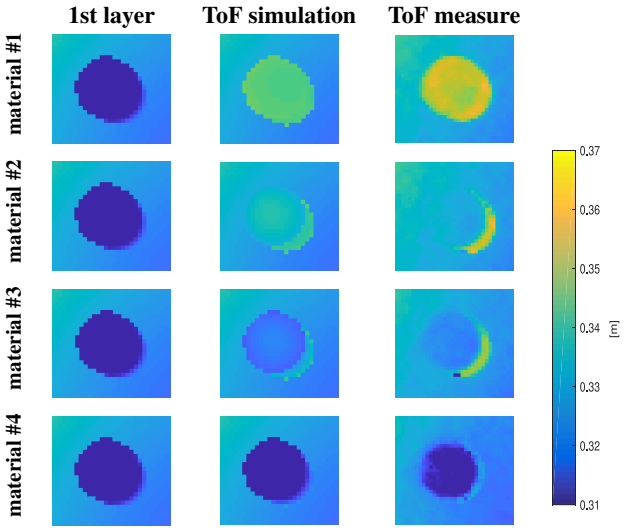

Figure 6: ***Scene 3** for materials with different absorption and scattering properties. The more transparent the material is the larger the distance value and thus the distance error becomes.*

ing. A large decrease of the scattering coefficent models **material #4** quite well. Due to the mixed in black color, the absorption of the material is large, while scattering effects vanish which leads to depth values similar to ground truth. In terms of our simulation this means that more random samples are placed next to the top plane of the cylinder. Still, this material causes an increase depth values at the sides of the cylinder which is also captured by our simulation. Tab. 2 summarized the empirically deduced materials parameters. Fig. 6 shows that our simulation models the qualitative refraction behavior of semi-transparent materials very well. The incident light at the side of the cylinders leads to an increased depth estimation due to the refracted light paths within the materials. Our simulation captures this behavior which is reflected by the larger depth values at the side of the cylinders compared to the to plane.

Fig. 7 demonstrates the influence of the material parameters on the simulation result. The first row shows the impact of the absorption coefficient σ_a. An increase of absorption decreases the radiance that is transfered within the geometry so that the amplitude of this radiance is quite low and the direct reflection dominates. The second row shows the the influence of σ_s. An increase implies stronger scattering contribution to the overall depth and thus an increase in depth. The third row show the effect of the scattering parameter g that defines how the phase function p behaves. Negative values cause a stronger back scattering and thus the samples in the simulation have a strong back scattering effect i.e. they have a larger overall contribution to the final superposition of signals. This implies an overall increase of the depth simlation values. hus, the depth values converge to the ground truth depth. The fourth row shows the effect of the refraction index η. It strongly influences the refraction direction considered in our simulation and thus the effect of corresponding path length. An increase of the refraction index causes longer paths to have a stronger effect, which leads to an increase in the overall depth simulation. On our computer (Intel i7-4720HQ 2.60GHz, NVIDIA GTX 980M) the simulation takes approx. 50 ms for computation of the superposition of direct, scattered and reflected radiance in the presented scenes.

7. Conclusion

In this paper we presented a simulation method for AMCW-ToF cameras that allows to capture subsurface scattering effect. Our method utilized screen space rasterization techniques to allow interactive frame rates. We use a multilayered G-Buffer to place random samples according to the absorption property within a homogeneous semi-transparent material. In contrast to common BSSRDF approaches our method includes an explicit evaluation of points withing the material and thus allows to integrate path lengths calculations required for a ToF simulation.

Furthermore, we have showed that our method can reproduce real world materials and scenarios sufficiently well. Common material properties like absorption, refraction and scattering can be set to mimic real materials and model their behavoir in our simulation.

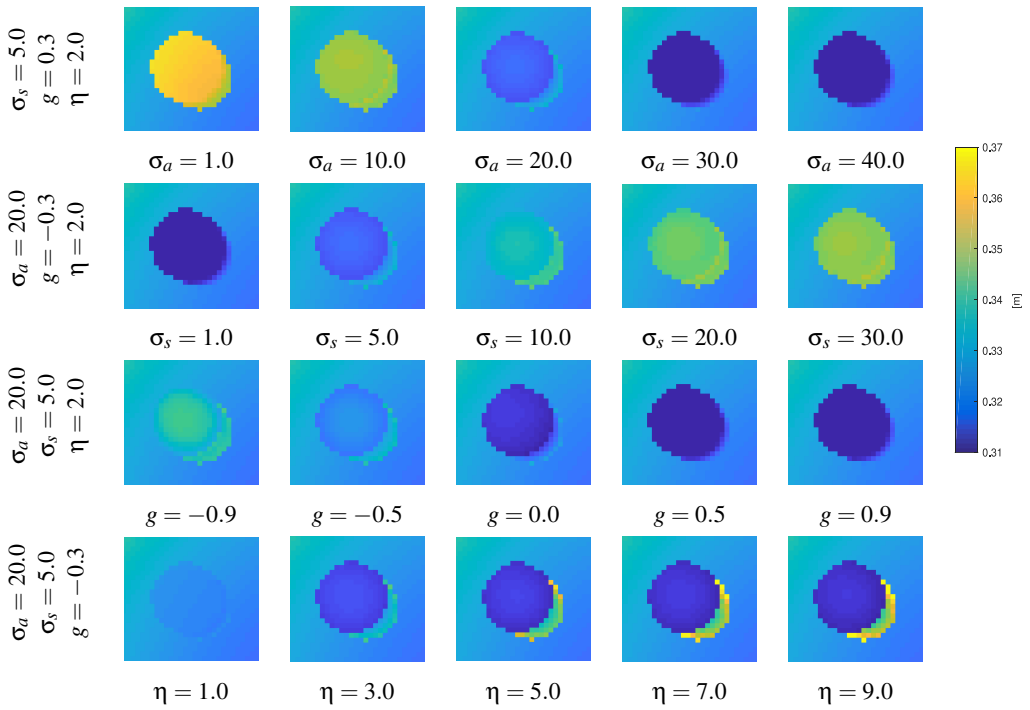

Figure 7: *Each row shows the impact of each parameter on the depth value simulation in* ***Scene 3*** *while all other material parameters are fixes (left column). From top to bottom the influence of* σ_a, σ_s, g *and* η *are shown.*

Acknowledgments: The work is partially funded by the German Research Foundation (DFG), grants Ko-2960-12/1 and GRK-1564/2.

References

[BLK17] BULCZAK D., LAMBERS M., KOLB A.: Quantified, interactive simulation of AMCW ToF camera including multipath effects. *Sensors 18*, 1 (2017). 1

[DLR*09] DONNER C., LAWRENCE J., RAMAMOORTHI R., HACHISUKA T., JENSEN H. W., NAYAR S.: An empirical BSSRDF model. *ACM Trans. Graph. 28*, 3 (2009), 30:1–30:10. 2

[ERS13] ELEK O., RITSCHEL T., SEIDEL H.-P.: Real-time screen-space scattering in homogeneous environments. *IEEE Comput. Graph. Appl. 33*, 3 (2013), 53–65. 2

[HG41] HENYEY L. G., GREENSTEIN J. L.: Diffuse radiation in the galaxy. *The Astrophysical Journal 93* (1941), 70–83. 3

[Inf15] INFINEON: Real3 (tm) image sensor family - 3D depth sensing based on time-of-flight. http://www.infineon.com/dgdl/Infineon-REAL3%20Image%20Sensor%20Family-PB-v01_00-EN.PDF?fileId=5546d462518ffd850151a0afc2302a58, 2015. 3

[Ish78] ISHIMARU A.: *Wave propagation and scattering in random media*. Academ. Press, 1978. 2

[JMLH01] JENSEN H. W., MARSCHNER S. R., LEVOY M., HANRAHAN P.: A practical model for subsurface light transport. In *Proc. SIGGRAPH* (2001), Proc. SIGGRAPH, ACM, pp. 511–518. 2

[JZJ*15] JIMENEZ J., ZSOLNAI K., JARABO A., FREUDE C., AUZINGER T., WU X.-C., VON DER PAHLEN J., WIMMER M., GUTIERREZ D.: Separable subsurface scattering: Separable subsurface scattering. *Comput. Graph. Forum 34*, 6 (2015), 188–197. 2

[LHK15] LAMBERS M., HOBERG S., KOLB A.: Simulation of Time-of-Flight sensors for evaluation of chip layout variants. *Sensors Journal, IEEE 15*, 7 (2015), 4019–4026. 1

[Max95] MAX N.: Efficient light propagation for multiple anisotropic volume scattering. In *Photorealistic Rendering Techniques*. Springer, 1995, pp. 87–104. 2

[MHM*18] MARCO J., HERNANDEZ Q., MUÑOZ A., DONG Y., JARABO A., KIM M., TONG X., GUTIERREZ D.: Deeptof: Off-the-shelf real-time correction of multipath interference in time-of-flight imaging. *CoRR abs/1805.09305* (2018). arXiv:1805.09305. 1

[MNK13] MEISTER S., NAIR R., KONDERMANN D.: Simulation of time-of-flight sensors using global illumination. In *Proc. Int. Conf. Vision, Modeling and Visualization (VMV)* (2013). doi:10.2312/PE.VMV.VMV13.033-040. 1

[NAM*17] NALBACH O., ARABADZHIYSKA E., MEHTA D., SEIDEL H.-P., RITSCHEL T.: Deep shading: Convolutional neural networks for screen space shading. *Comput. Graph. Forum 36*, 4 (2017), 65–78. 2

[NML*13] NAIR R., MEISTER S., LAMBERS M., BALDA M., HOFFMANN H., KOLB A., KONDERMANN D., JÄHNE B.: *Time-of-Flight and Depth Imaging*, vol. 8200 of *LNCS*. Springer, 2013, ch. Ground Truth for Evaluating Time of Flight Imaging, pp. 52–74. 1

[PAT*04] PREMOŽE S., ASHIKHMIN M., TESSENDORF J., RAMAMOORTHI R., NAYAR S.: Practical rendering of multiple scattering effects in participating media. In *Proc. Eurographics* (2004), pp. 363–374. 2, 4

[RT87] RUSHMEIER H. E., TORRANCE K. E.: The zonal method for calculating light intensities in the presence of a participating medium. In *ACM SIGGRAPH Computer Graphics* (1987), vol. 21, ACM, pp. 293–302. 2

[SHWH18] SU S., HEIDE F., WETZSTEIN G., HEIDRICH W.: Deep end-to-end time-of-flight imaging. 1